Electronic Supplementary Material (ESI) for Nanoscale.

Thermal conductivity of benzothieno-benzothiophene derivatives at the nanoscale

Magatte N. Gueye,[a,#] Alexandre Vercouter,[b,#] Rémy Jouclas,[c] David Guérin,[a]

Vincent Lemaur,[b] Guillaume Schweicher[c,],[c] Stéphane Lenfant,[a]*

Aleandro Antidormi,[d] Yves Geerts,[c,e] Claudio Melis,[f]

Jérôme Cornil[b,] and Dominique Vuillaume[a,*]*

a) Institute for Electronics Microelectronics and Nanotechnology (IEMN), CNRS, Av. Poincaré, Villeneuve d'Ascq, France.

b) Laboratory for Chemistry of Novel Materials, University of Mons, Place du Parc 20, Mons, Belgium.

c) Laboratoire de Chimie des Polymères, Faculté des Sciences, Université Libre de Bruxelles (ULB), Boulevard du Triomphe, 1050, Brussels, Belgium.

d) Catalan Institute of Nanoscience and Nanotechnology (ICN2), CSIC and BIST, Campus UAB, Bellaterra, 08193, Barcelona, Spain.

e) International Solvay Institutes for Physics and Chemistry, Brussels, Belgium.

f) Dipartimento di Fisica, Universita di Cagliari, Cittadella Universitaria, 09042 Monserrato (Ca), Italy.

Corresponding authors: dominique.vuillaume@iemn.fr ; guillaume.schweicher@ulb.ac.be ; jerome.cornil@umons.ac.be

Supporting information

1. Sample fabrication
2. SThM measurements
3. Theoretical methods
4. Additional SThM images
5. NP-SThM calibration
6. Estimation of the constriction thermal resistance of the Si/SiO_2 substrate

7. Estimation of the radius of the thermal contact between tip and surface
8. Fitted parameters of Eq. 3.

1. Sample fabrication

The Si-n^+(highly doped ~10^{-3} Ω.cm)/SiO_2 substrate (200 - 500 nm of thermal SiO_2) were first cleaned in CH_2Cl_2 (3mn, sonicated), in IPA (isopropyl alcohol) solution (3mn, sonicated) and then submitted during 10 mn to UV-ozone cleaning. They were used immediately. The C8-BTBT-C8 and BTBT (scheme 1) solutions (5mg/mL in toluene for BTBT and 5 mg/mL in tetrahydrofuran for C8-BTBT-C8) were spin coated at 1000 rpm for 9s followed by 30 s at 1500 rpm, or directly at 4500 rpm for 30 s. We used two methods to deposit a drop of the solution onto the substrate: we dropped the solution on the substrate and started the spin-coater (method A) or we dropped the solution while the spin coater was already running (method B). Table S1 summarizes the spin-coating conditions for the 9 samples. The films are not uniform and we have indicated the maximum thickness of the films as measured from AFM images (see Figs. S1 and S2).

	C8-BTBT-C8		BTBT	
#1	1000 rpm/9 s + 1500 rpm/30s (method A)	410 nm	4500 rpm/30s (method B)	360 nm
#2	1000 rpm/9 s + 1500 rpm/30s (method B)	160 nm	4500 rpm/30s (method A)	360 nm
#3	4500 rpm/30s (method A)	190 nm	4500 rpm/30s (method B)	320 nm
#4	4500 rpm/30s (method B)	90 nm	4500 rpm/30s (method A)	390 nm
#5	1000 rpm/9 s + 1500 rpm/30s (method B)	390 nm		

Table S1. *Spin-coating parameters and maximum film thickness (rounded to the unit) estimated from AFM measurements.*

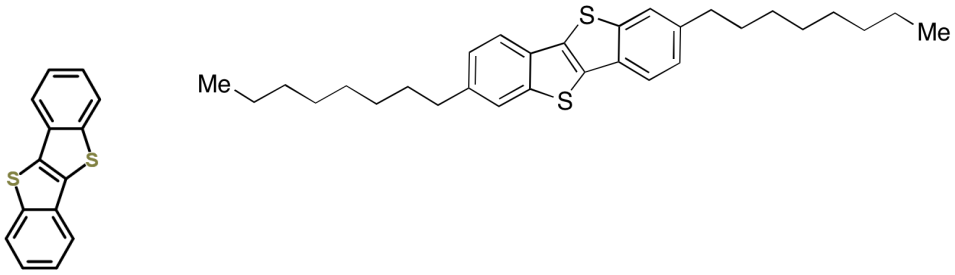

Scheme S1. *Chemical structures: BTBT (left) and C8-BTBT-C8 (right), Me=CH_3.*

2. SThM measurements

Topographic and thermal images*.* In the scanning mode, the topography and thermal voltage were recorded simultaneously. We used both the DC method or the 3ω-SThM. The SThM tip is a lithographed Pd wire, i.e. resistance, inserted in a Wheatstone bridge, which is supplied by a DC voltage, V_{DC}. The tip is used to heat the sample (the higher the DC voltage, the higher the heat flux and the tip temperature) and to measure the tip/surface temperature, in the so-called active mode. The tip resistance is measured by the Wheatstone bridge connected to a voltage amplifier. From this output SThM voltage, we deduced the tip resistance, which is calibrated versus temperature. Thus, the SThM voltage recorded at the amplifier output can be converted to tip/sample temperature. To minimize parasitic contributions (air conduction, radiation) and thus increase the sensitivity of the tip/sample contribution, we also use the 3ω-SThM method,[1, 2] in which the Wheatstone bridge is supplied by an AC voltage (0.2 V at 1 kHz) and we measure the third harmonic signal at the Wheatstone bridge output with a lock-in.

Null-point SThM method*.* The null-point SThM[3] was used at selected points on the organic films (organic domains) and/or the uncovered Si/SiO_2 substrate. From a previously recorded topographic/thermal image a zone of interest is selected where we define a 5x5 grid, each point spaced by 10 nm. At each point of the grid, in the z-trace mode (approach and retract) we recorded the SThM voltage

versus distance curve (V_{SThM}-z). At the transition from a non-contact (NC, tip very near the surface) to a contact (C, tip on the surface) situation, we observe a temperature jump, T_{NC} - T_C, which is used to determine the sample thermal conductivity according to the protocol described in Ref. 3. The temperature jump is measured from the approach trace only (to avoid any artifact due to well-known adhesion hysteresis of the retract curve) and averaged over the 25 recorded V_{SThM}-z traces. This differential method is suitable to remove the parasitic contributions (air conduction, etc…): at the contact (C) both the sample and parasitic thermal contributions govern the V_{SThM} signal, whereas, just before physical tip contact (NC), only the parasitic thermal contributions are involved. The plot of the temperature jump, T_{NC} - T_C, versus the sample temperature at contact T_C is linear and its slope is inversely proportional to the thermal conductivity. The tip-sample temperature T_C increases with the supply voltage of the Wheatstone bridge V_{DC} (typically from 0.4 to 1 V).

Thermal flux. The determination of the thermal resistance from the ratio of the thermal voltage measured on the organic domain versus over the substrate is valid under the hypothesis that all the electrical power delivered to the tip is dissipated into the sample and the thermal flux is constant.[4, 5] Albeit not strictly verified, this is justified, in first approximation, since the constriction resistances on the two zones are quite similar around 10^7 K W^{-1} ($R_{sub}=1/4r\mathcal{K}_{ox}$ = 9x10^6 K W^{-1}, $R_{org}=1/4r\mathcal{K}_{org}$ = 2-5x10^7 K W^{-1}, considering the values of $\mathcal{K}_{org}$ determined by the NP-SThM). However, in addition to taking into account the interface resistances (see text), a more precise analysis of data in Fig. 3 implies that a correction factor should be applied to determine the ratio R^*_{org}/R_{sub} from the ratio of the SThM voltages, $R^*_{org}(t)/R_{sub} = \left(V_{SThm-org}/V_{SThM-sub}\right)\left(\dot{Q}_{sub}/\dot{Q}_{org}\right)$. Since the thermal conductivity is lower for C8-BTBT-C8 than for BTBT, the correction factor $\dot{Q}_{sub}/\dot{Q}_{org}$ should be higher for C8-BTBT-C8.

3. Theoretical methods

Molecular Dynamics. A wide range of Molecular Dynamics (MD) simulations has been developed to assess the lattice thermal conductivity of a plethora of materials and complex nanostructures.[6, 7] Among them, the Green-Kubo (GK) formalism[8] based on the fluctuation-dissipation theorem provides a direct access to the (off-)diagonal elements of the two-dimensional thermal conductivity tensor. Nevertheless, ensuring the proper convergence of the auto- and cross-correlation functions of the heat current may be a non-trivial task, especially for soft molecular systems. A second class of techniques built on a Non-Equilibrium Molecular Dynamics (NEMD) scheme[9] requires important computational resources to artificially maintain the system out of equilibrium while estimating its thermal conductivity in a stationary state. The key steps of the AEMD methodology are the following: (i) applying a perfectly monitored thermal pulse on a simulation box; (ii) recovering the initial thermodynamic equilibrium during a fast transient regime; (iii) fitting the time-decaying temperature difference between the right and left parts of the system from a reliable solution of the one-dimensional heat equation $\frac{\partial T}{\partial t} = D\frac{\partial^2 T}{\partial x^2}$ in order to evaluate the thermal diffusivity, D.[10] This alternative scheme has the benefit to be far less time-consuming than the previously cited methods due to the rapid dissipation of the thermal gradient. The AEMD approach also contrasts with both the Equilibrium Molecular Dynamics (EMD) and the Non Equilibrium Molecular Dynamics (NEMD) techniques by estimating the phononic contribution to the thermal transport with no need for any instantaneous heat flux; moreover, the definition of the heat flux in the LAMMPS software[11] has been recently identified as physically inconsistent for the study of molecular systems.[12, 13] With the AEMD approach, the thermal conductivity $\kappa = D\rho C_P$ is finally obtained, provided the density, ρ, and the specific heat, C_P, of the system are known.[10] The parameter C_P is typically

estimated to be 3*R* (with *R* the ideal gas constant), as predicted by the Dulong-Petit model.[14] Note that no quantum corrections are taken into account because MD simulations are performed at 300K while many OSCs are characterized by a very low Debye temperature θ_D [15, 16] so that the classical approximation used in the Dulong-Petit relationship is still valid. It is also of prime importance to account for the size-dependence of the lattice thermal conductivity deduced from this approach since phonons having a mean free path larger than the cell dimension do not effectively contribute to κ. An extrapolation procedure is thus needed to get rid of these size effects[17] and to extract a quasi-length-free lattice thermal conductivity from the linear regression of $1/\kappa$ versus 1/L (L the length of the box size along the direction of heat propagation). We have carefully reparameterized the torsional potential terms against sophisticated quantum-chemical calculations, with atomic charges calculated at the 1.14*CM1A-LBCC level.[18] The implementation of the force field was insured by the LigParGen free server.[19] Supercells ranging from 10 to 52 units cell have been generated along each direction of interest for heat transport and periodic boundary conditions were applied along the main three axes. First, atomic positions were optimized at 0 K while keeping fixed the cell parameters before relaxing the whole simulation box during a second energy minimization. Afterwards, systems have been aged in the canonical NVT ensemble (mole (N), volume (V) and temperature (T)) and in the isothermal–isobaric NPT ensemble (mole (N), pressure (P) and temperature (T)) during 1 ns in ambient conditions, using a Nose-Hoover thermostat and barostat. Then, a step-like temperature profile was created by simultaneously "freezing" atomic motions in one half of the simulation box while heating up [cooling down, respectively] the second part of the system alternatively at < T1 > = 362.5 K (< T2 > = 237.5 K, respectively) via NVT simulations (~ 250 ps). Finally, an NVE (mole (N), volume (V) and energy (E)) simulation lasting up to ~ 3 ns was achieved to dissipate the initial 125 K thermal gradient. Throughout a post-

processing step, the monitored temperature offset $\Delta T = \langle T_1 \rangle - \langle T_2 \rangle$ was fitted by a sum of exponentials expressed as $\sum_{n=1}^{5} C_n e^{-\alpha_n^2 Dt}$, where C_n and α_n are coefficients depending on initial conditions. A fitting function based on five terms is the best compromise between reasonable computational time and sufficient accuracy for the estimation of the lattice thermal conductivity.

Estimation of the participation ratio. In order to characterize the vibrational properties of both BTBT and C8-BTBT-C8, we performed the diagonalization of the corresponding dynamical matrix given by:

$$D_{i\alpha,j\beta} = \frac{-1}{\sqrt{m_i m_j}} \frac{\partial F_{i\alpha}}{\partial r_{j\beta}} \qquad \text{(s1)}$$

where m_i is the mass of the i^{th} atom, $F_{i\alpha}$ is the force on the i^{th} atom along the α direction due to a displacement of atom j along the β direction. Latin indices are used for labelling atoms while Greek letters indicate the (x,y,z) Cartesian components. The diagonalization of the dynamical matrix was obtained by using the SLEPc library[20] in order to obtain the eigenvectors e_s and eigenvalues ω^2_s where s = 1, . . . ,3N counts the system eigenmodes. The calculation of the force first derivatives have been performed using a numerical finite difference procedure by considering an atomic displacement as small as 5 x 10^{-4} Å. Once the eigenvectors have been calculated, we estimated the participation ratio (PR) as:[21]

$$PR = \frac{1}{N} \frac{\left(\sum_{i=1}^{N} {e_{i,s}}^2 \right)^2}{\sum_{i=1}^{N} {e_{i,s}}^4} \qquad \text{(s2)}$$

PR yields an estimation of the contribution of a subgroup of atoms in a specific vibrational mode. The actual localized or extended character of that mode is

related to the actual PR value: PR ~ 1 in the case of extended modes while PR has a smaller value for localized modes. It is worth noticing that, according to its very definition, a PR exactly equal to unity is obtained solely for vibrational modes in ideally perfect crystalline systems, in which the atomic displacements are perfectly periodic within the sample. In general, the PR values for extended modes in non-crystalline systems lie in the 0.4- 0.6 interval.

4. Additional SThM images

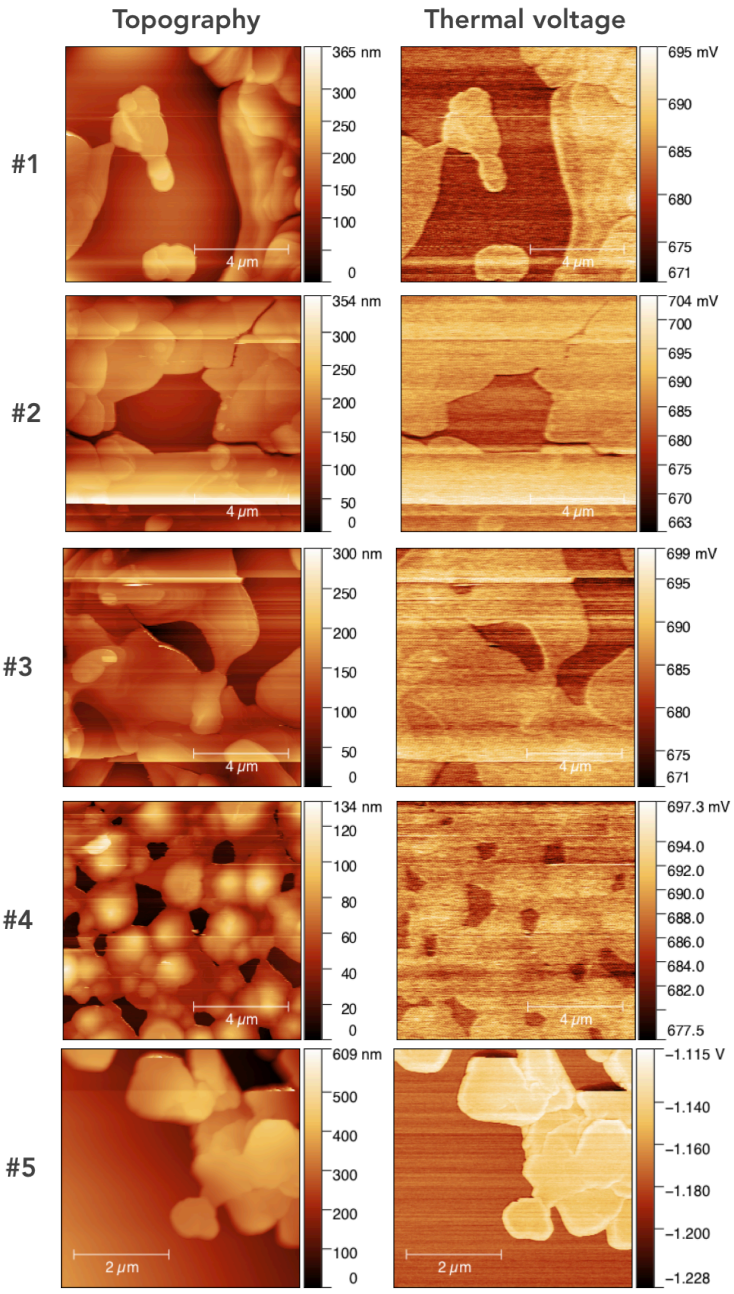

Figures S1. *Typical topographic and thermal voltage images of the five C8-BTBT-C8 measured by 3ω-SThM (V_{AC} = 0.2 V, 1 kHz), samples #1-4, and by DC-SThM (V_{DC} = 0.5V), sample #5.*

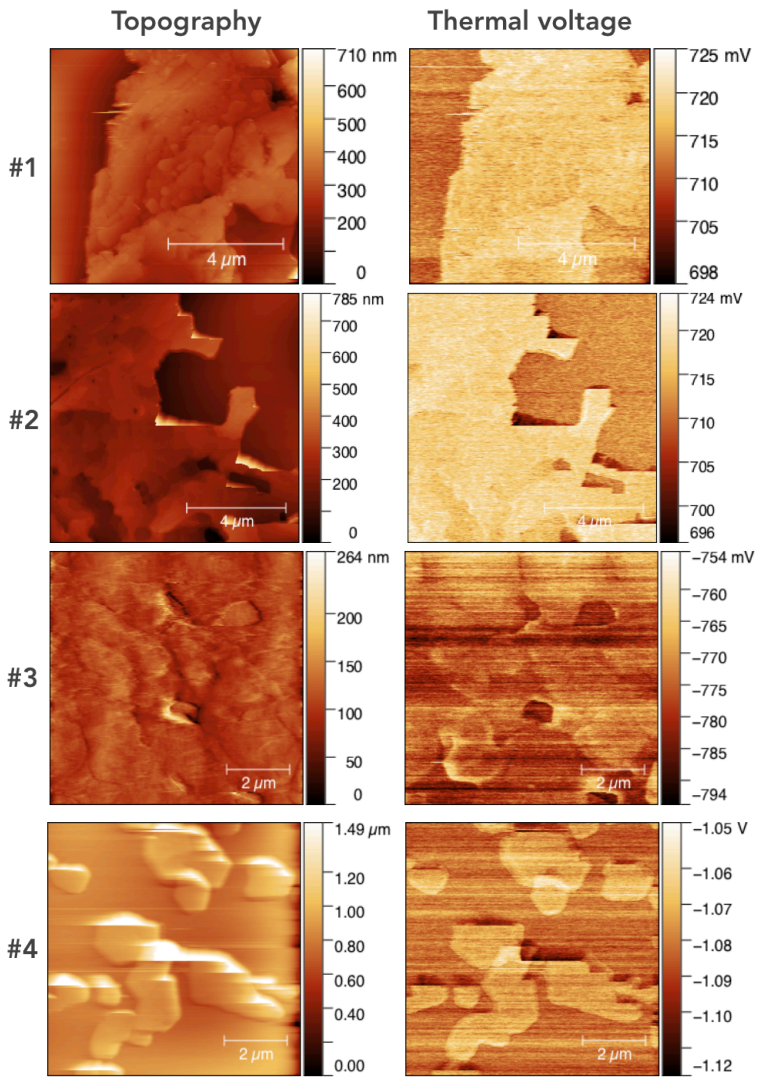

Figure S2. *Typical topographic and thermal voltage images of the BTBT samples measured by 3ω-SThM (V_{AC} = 0.2 V, 1 kHz) for samples #1 and 2 and samples #3,4 by DC-SThM (V_{DC} = 0.6V).*

5. NP-SThM calibration.

The sample temperature is calculated from the measured thermal voltage by

$$V_{SThM} = GR_{tip}\left(T_{sample}\right) = G\left[R_{amb} + \lambda\left(T_{sample} - T_{amb}\right)\right] \qquad \text{(Eq.S1)}$$

where G is the known transfer function of the Wheatstone bridge and the amplifier gain (1.08 x V_{DC} V/Ω) for the DC-SThM methods,[22] 8.2x10^{-2} x V_{AC} V/Ω for the 3ω-SThM. The tip resistance R_{tip} varies linearly with sample temperature, and has been calibrated given R_{amb}= 290.2 Ω and λ = 0.27 Ω/°C.

To determine the thermal conductivity from data in Fig. 3 and using Eq. (2), we calibrated the null-point SThM according to the protocol in Ref. 3. The same T_C vs. T_{NC}-T_C measurements were done on two materials with well-known thermal conductivity (below) : a glass slide (1.3 W/m.K) and a low doped silicon wafer with its native oxide (150 W/m.K). From a linear fit on the data, we get α = 25.6 W m^{-1} K^{-1} and β = 21.6 K/K.

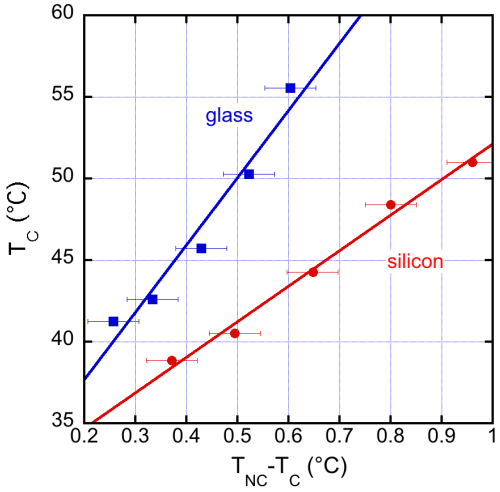

Figure S3. *T_C vs. T_{NC} - T_C plot for the two reference materials. Solid lines are the linear fits.*

6. Estimation of the constriction thermal resistance of the Si/SiO_2 substrate

The effective thermal conductivity measured by NP-SThM is the one of the bulk SiO_2 (see Fig. 6-b in Ref. 3 and below) if the SiO_2 thickness is larger than ~ 100 nm (here 200-500 nm).[3] This behavior is in agreement with a simple analytical model derived by Dryden[23] for film with *t/r* > 2 (*r* being the radius of the SThM tip

thermal contact ($r \approx 20$ nm, see below). Thus, we used for the Si/SiO_2 substrate $R_{sub}=1/4r\kappa_{OX}$ = 9x10^6 K W^{-1} with κ_{OX} the "bulk" SiO_2 thermal conductivity (1.4 W m^{-1} K^{-1}).

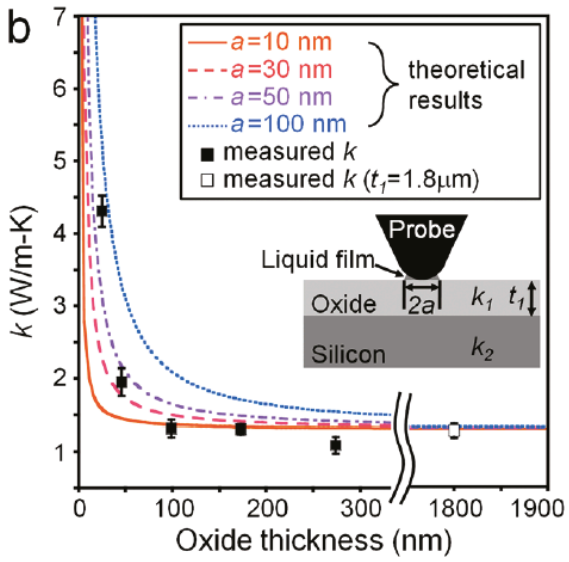

Figure S4. *Variation of the measured thermal conductivity of a silicon substrate covered by a film of SiO_2 with various thickness (Reprinted with permission from Kim, K.; Chung, J.; Hwang, G.; Kwon, O.; Lee, J. S. ACS Nano 2011, 5, 8700–8709. Copyright (2011) American Chemical Society).*

7. Estimation of the radius of the thermal contact between tip and surface.

The thermal contact radius is calculated following the approach reported in Ref. 24 taken into account the mechanical tip radius r_{tip} and the size of the water meniscus at the tip/surface interface. The thermal radius of the thermal contact is given by [25]

$$r_{th} = 2.08\sqrt{\frac{-r_{tip}\cos\theta}{\ln\varphi}} \qquad \text{(Eq. S2)}$$

with r_{tip} = 100 nm (data from Bruker), the relative humidity φ = 0.35-0.4 (air-conditioned laboratory, values checked during the measurements) and the contact angle of the concave meniscus between the tip and the surface $\theta \approx 30°$ as measured for π-conjugated molecular crystals in Ref. 26. We get r ≈ 20 nm. The water meniscus contact angle depends on the surface energy of the sample, and thus should, in principle, not be the same on the organic domains and the uncovered SiO_2 surface, the later being more hydrophilic than the organic materials. However, we cannot perform standard water contact angle measurements inside the micrometer size uncovered SiO_2 (see Fig. S1 and S2), and we consider the same value of 30° in both cases. Moreover, it is likely that the SiO_2 surface is covered by organic contaminants from the spin-coating deposition technique.

8. Fitted parameters of Eq. 3.

Table S2 gives the values of the fitted parameters (κ_{org}) for the data shown in Fig. 4 (main text).

	C8-BTBT-C8	**BTBT**
	K_{org} *(W m^{-1} K^{-1})*	K_{org} *(W m^{-1} K^{-1})*
sample #1	1.348	1.371
sample #2	1.352	1.373
sample #3	1.359	1.366
sample #4	1.355	1.372

Table S2. *Fit parameters (Fig. 4, Eq. 3)*

We get the average values κ_{BTBT} = 1.37 ± 0.01 W m^{-1} K^{-1} and $\kappa_{C8\text{-}BTBT\text{-}C8}$ = 1.35 ± 0.01 W m^{-1} K^{-1}. We note that a values of *r* = 80 nm has been used to these fits. Using *r* = 20 nm gave poor fits. The value *r* = 80 nm should indicate a more

hydrophilic surface (Eq. S2, lower θ, but Eq. (S2) has a limit r = 21.7 nm for θ=0°, thus this simple model is inappropriate in the case of highly hydrophilic surface). Nevertheless, this uncertainty in the determination of *r* does not change the conclusion of the NP-SThM measurements that the thermal conductance of BTBT is higher than for C8-BTBT-C8 (r is included in the calibration parameters).

References

1. Lefèvre, S.; Volz, S., 3ω-scanning thermal microscope. *Rev. Sci. Instrum.* **2005,** *76* (3), 033701.

2. Bodzenta, J.; Juszczyk, J.; Chirtoc, M., Quantitative scanning thermal microscopy based on determination of thermal probe dynamic resistance. *Rev. Sci. Instrum.* **2013,** *84* (9), 093702.

3. Kim, K.; Chung, J.; Hwang, G.; Kwon, O.; Lee, J. S., Quantitative measurement with scanning thermal microscope by preventing the distortion due to the heat transfer through the air. *ACS Nano* **2011,** *5* (11), 8700-8709.

4. Menges, F.; Riel, H.; Stemmer, A.; Gotsmann, B., Quantitative Thermometry of Nanoscale Hot Spots. *Nano Lett* **2012,** *12*, 596-601.

5. Meier, T.; Menges, F.; Nirmalraj, P.; Hölscher, H.; Riel, H.; Gotsmann, B., Length-Dependent Thermal Transport along Molecular Chains. *Phys. Rev. Lett.* **2014,** *113* (6), 060801.

6. Fugallo, G.; Colombo, L., Calculating lattice thermal conductivity: a synopsis. *Physica Scripta* **2018,** *93* (4), 043002.

7. Puligheddu, M.; Xia, Y.; Chan, M.; Galli, G., Computational prediction of lattice thermal conductivity: A comparison of molecular dynamics and Boltzmann transport approaches. *Physical Review Materials* **2019,** *3* (8), 085401.

8. Kubo, R.; Toda, M.; Hashitsume, N., *Statistical Physics II*. Spinger: Berlin, 1985.

9. Müller-Plathe, F., A simple nonequilibrium molecular dynamics method for calculating the thermal conductivity. *The Journal of Chemical Physics* **1997,** *106* (14), 6082-6085.

10. He, Y.; Savić, I.; Donadio, D.; Galli, G., Lattice thermal conductivity of semiconducting bulk materials: atomistic simulations. *Physical Chemistry Chemical Physics* **2012,** *14* (47), 16209-16222.

11. Plimpton, S., Fast Parallel Algorithms for Short-Range Molecular Dynamics. *Journal of Computational Physics* **1995,** *117* (1), 1-19.

12. Boone, P.; Babaei, H.; Wilmer, C. E., Heat Flux for Many-Body Interactions: Corrections to LAMMPS. *Journal of Chemical Theory and Computation* **2019,** *15* (10), 5579-5587.

13. Surblys, D.; Matsubara, H.; Kikugawa, G.; Ohara, T., Application of atomic stress to compute heat flux via molecular dynamics for systems with many-body interactions. *Physical Review E* **2019,** *99* (5), 051301.

14. Ashcroft, N. W.; Mermin, N. D., *Solid State Physics*. HoltSander: London, 1976.

15. Ramadoss, P.; Buvaneswari, N., Thermal Properties of Some Organic Liquids Using Ultrasonic Velocity Measurements. *E-Journal of Chemistry* **2011,** *8*, 120260.

16. Babavali, S. F.; Nori, T. S.; Srinivasu, C., Acoustical effective Debye temperature studies in heterocyclic aromatic functional materials of organic liquid mixtures at four different temperatures T = (303.15, 308.15, 313.15 and 318.15) K. *Materials Today: Proceedings* **2019,** *18*, 2073-2076.

17. Sellan, D. P.; Landry, E. S.; Turney, J. E.; McGaughey, A. J. H.; Amon, C. H., Size effects in molecular dynamics thermal conductivity predictions. *Physical Review B* **2010,** *81* (21), 214305.

18. Dodda, L. S.; Vilseck, J. Z.; Tirado-Rives, J.; Jorgensen, W. L., 1.14*CM1A-LBCC: Localized Bond-Charge Corrected CM1A Charges for Condensed-Phase Simulations. *The Journal of Physical Chemistry B* **2017,** *121* (15), 3864-3870.

19. Dodda, L. S.; Cabeza de Vaca, I.; Tirado-Rives, J.; Jorgensen, W. L., LigParGen web server: an automatic OPLS-AA parameter generator for organic ligands. *Nucleic Acids Research* **2017,** *45* (W1), W331-W336.

20. Hernandez, V.; Roman, J. E.; Vidal, V., SLEPc: A Scalable and Flexible Toolkit for the Solution of Eigenvalue Problem. *ACM Trans. Math. Softw.* **2005,** *31*, 351-362.

21. Antidormi, A.; Cartoixà, X.; Colombo, L., Nature of microscopic heat carriers in nanoporous silicon. *Physical Review Materials* **2018,** *2* (5), 056001.

22. Anasys-Instruments SThM installation and operation manual; 2008.

23. Dryden, J. R., The Effect of a Surface Coating on the Constriction Resistance of a Spot on an Infinite Half-Plane. *J. Heat Transfer* **1983,** *105*, 408-410.

24. Luo, K.; Shi, Z.; Varesi, J.; Majumdar, A., Sensor nanofabrication, performance, and conduction mechanisms in scanning thermal microscopy. *Journal of Vacuum Science & Technology B: Microelectronics and Nanometer Structures* **1997,** *15* (2), 349-360.

25. Israelachvili, J. N., Intermolecular and surface forces; 3rd ed. Academic Press: Amsterdam, 2011.

26. Zhang, Y.; Zhang, C.; Wei, D.; Bai, X.; Xu, X., Nanoscale thermal mapping of few-layer organic crystal. *CrystEngComm* **2019,** *21*, 5402-5409.